Current Optics and Photonics
Vol. 2, No. 1, February 2018, pp. 69-78

ISSN: 2508-7266(Print) / ISSN: 2508-7274(Online)
DOI: https://doi.org/10.3807/COPP.2018.2.1.069

Precise Edge Detection Method Using Sigmoid Function in Blurry and Noisy Image for TFT-LCD 2D Critical Dimension Measurement

Seung Woo Lee, Sin Yong Lee, and Heui Jae Pahk*

School of Mechanical and Aerospace Engineering, Seoul National University, Seoul 08826, Korea

(Received May 11, 2017 : revised October 24, 2017 : accepted November 29, 2017)

This paper presents a precise edge detection algorithm for the critical dimension (CD) measurement of a Thin-Film Transistor Liquid-Crystal Display (TFT-LCD) pattern. The sigmoid surface function is proposed to model the blurred step edge. This model can simultaneously find the position and geometry of the edge precisely. The nonlinear least squares fitting method (Levenberg-Marquardt method) is used to model the image intensity distribution into the proposed sigmoid blurred edge model. The suggested algorithm is verified by comparing the CD measurement repeatability from high-magnified blurry and noisy TFT-LCD images with those from the previous Laplacian of Gaussian (LoG) based sub-pixel edge detection algorithm [1] and error function fitting method [7]. The proposed fitting-based edge detection algorithm produces more precise results than the previous method. The suggested algorithm can be applied to in-line precision CD measurement for high-resolution display devices.

Keywords : TFT-LCD, Critical dimension measurement, Edge detection, Levenberg-Marquardt fitting, Blur edge modeling

OCIS codes : (100.2000) Digital image processing; (120.3940) Metrology; (150.3045) Industrial optical metrology

I. INTRODUCTION

Thin-Film Transistor Liquid-Crystal Displays (TFT-LCD) have been widely used as displays for devices such as laptops, smartphones, and monitors. The manufacturing inspection and process control of TFT-LCDs are mostly done by two-dimensional critical dimension (2D CD) measurement. The 2D CD measurement, nowadays, requires repeatability of several tens of nanometers, and therefore a high precision measurement system is required. The TFT-LCD pattern is getting smaller to make high-resolution display devices. Therefore, a high magnification optical system is required to measure the CDs of the integrated pattern.

2D CD measurement is based on the edge detection of TFT pattern image having two-dimensional geometries (e.g. line width, circle diameter), being captured by a CCD camera. Therefore, edge detection is important in the 2D CD measurement. The repeatability is strongly affected by the precision and robustness of the edge detection algorithm. Due to the optical limitations such as optical blurring and noise of camera sensor, the 2D CD measurement, however, has lots of difficulty in trying to obtain better precision and higher magnification [2, 3].

Edge detection of an image is to detect the pixel position where the intensity contrast is large. There have been several previous edge detection methods: max gradient methods were traditionally used to obtain the first or second order gradient of an image, gray moment methods [4, 5] were adopted to calculate the intensity distribution of the image, and curve fitting methods [6-8] were used to model the intensity distribution of the image with a specific function.

The max gradient methods calculate intensity slope at each pixel and detect the pixel having a maximum slope as the edge position, and they include the Sobel mask [9], Laplacian of Gaussian (LoG) mask [10], Canny edge detection [11], etc. The max gradient methods were widely used

*Corresponding author: hjpahk@snu.ac.kr, ORCID 0000-0002-3838-6928

Color versions of one or more of the figures in this paper are available online.

This is an Open Access article distributed under the terms of the Creative Commons Attribution Non-Commercial License (http://creativecommons.org/licenses/by-nc/4.0/) which permits unrestricted non-commercial use, distribution, and reproduction in any medium, provided the original work is properly cited.

Copyright © 2018 Current Optics and Photonics

because of their simple and easy calculations, and many popular 2D CD measurement algorithms in TFT-LCD were also based on the maximum gradient [1, 2]. Those methods are, however, very sensitive to noise and blur of the image. As the max gradient methods search the maximum slope position in pixel level, the sub-pixel edge-searching algorithm should be added for more precise edge detection.

The gray moment methods estimate the boundary position through the statistical analysis of the image intensity distribution [4, 5]. It can estimate the edge position precisely even though the edge is blurred. As the gray moment methods estimate the edge position statistically, the precise edge detection is possible at the sub-pixel level. But, it may have difficulty in localizing the true edge position when the noise is large or other TFT patterns are overlapped around the region of interest (ROI). For the other types of edges such as roof edge or line edge, it is also difficult to detect the edge position statistically.

The curve fitting methods are to estimate the edge position by modeling a blurred edge with a specific function [7, 8]. The error function (integration of Gaussian function) [7] and piecewise cubic polynomial [8] were used in the previous study. These methods also have some advantage in measuring blurred edges and sub-pixel level edge positioning. Those methods used in previous research, however, can only be applied to 1D intensity profiles. Therefore, to know the boundary position of the image by using those methods, it is necessary to perform fitting operations on multiple profiles. Since the fitting operation has to be repeated for each profile, the conventional methods have a limitation in that they take a long time to converge. In addition, these methods are focused only on straight line boundaries and have limitations for detecting various boundaries, such as circle or ellipse.

In this study, to overcome the limitations of edge detection in noisy and blurry images, a new edge detection method is suggested when the blurred step edge is modeled as a sigmoid function. In particular, the proposed method models the intensity of image as two-dimensional intensity data, rather than modeling the simple intensity profile of the image. The non-linear least squares fitting method (Levenberg-Marquardt method) is also used to model the image intensity distribution into the proposed sigmoid blurred edge model. From this modeling, the geometry of the image edge can be calculated mathematically. By using this mathematical information about geometry, the 2D CD, therefore, can be measured more precisely.

II. BLURRED EDGE MODELING BY SIGMOID FUNCTION

2.1. Blurred Edge Model in Highly Magnified Images

A standard grid sample, as shown in Fig. 1, is used to verify the effect of the image blur. Figures 1(a) and 1(b) show a typical image of the 20µm standard grid in 20X and 50X respectively. In Fig. 1, the arrows indicate the normal direction of the edge for intensity profile and the rectangle is the region of interest (ROI). Figure 2 shows the intensity profile along the arrow direction of standard grid sample in 20X, 50X magnification. The intensity distribution around the edge of the blurred image shows the S-shaped curve and the edge gets more blurred as the optical magnification increases. Figure 3 shows the intensity distribution of 50X magnified image in three dimensions. Due to the blur and noise effect in the image shown in

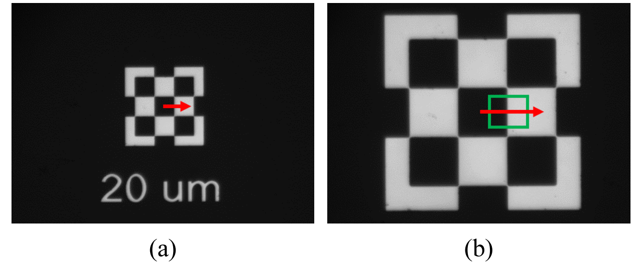

FIG. 1. Image of 20 µm standard grid sample in 20X, 50X magnification. (a) Image in 20X. (b) Image in 50X.

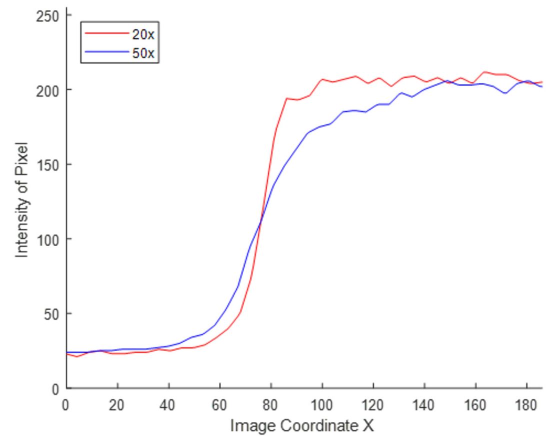

FIG. 2. Intensity profile of standard grid sample's edge in 20X, 50X magnification.

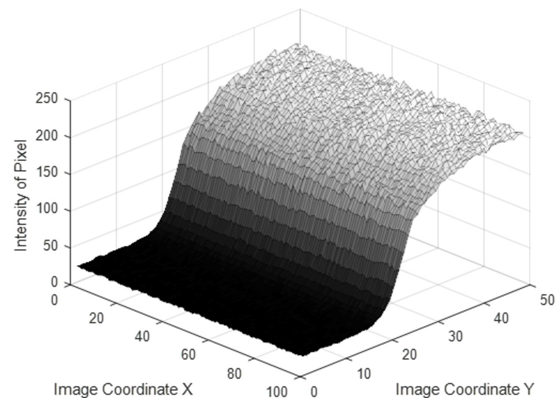

FIG. 3. Intensity distribution of 50X magnified image in three dimensions.

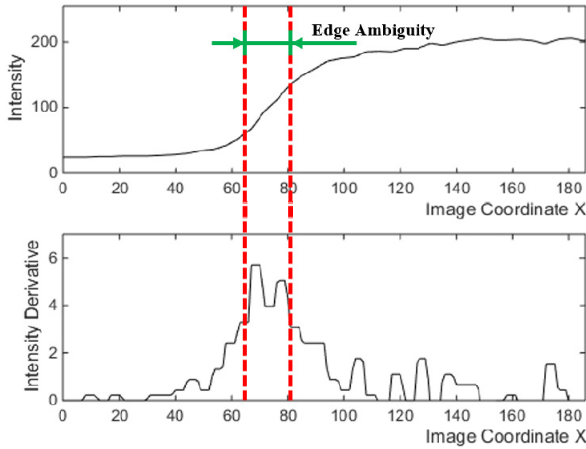

FIG. 4. Intensity and derivative of intensity along the edge normal direction of the standard grid sample in 50X magnification.

Figs. 2 and 3, the ambiguity of edge detection increases. As the edge of an image is defined as the position of the steepest intensity change, the edge position cannot be accurately calculated by the steepest gradient method, where the edge ambiguity is observed as in Fig. 4. To overcome the ambiguity of edge detection, the sigmoid function is proposed to model the intensity distribution of the blurred edge.

2.2. Sigmoid Modeling

In this paper, the sigmoid function is proposed to model the simple blurred step edge. For the one-dimensional intensity profile, the sigmoid function can be expressed as Eq. (1) and the derivative at $x=-\frac{n}{m}$ is calculated as Eq. (2).

$$Z(x)=\frac{K}{1+\exp(mx+n)}+D \tag{1}$$

$$\left.\frac{dZ}{dx}\right|_{x=-\frac{n}{m}}=\left.\frac{-Km\exp(mx+n)}{(1+\exp(mx+n))^2}\right|_{x=-\frac{n}{m}}=\frac{-Km}{4} \tag{2}$$

where the intensity model function Z(*x*) is the function of x and, x is the variable along the direction of the intensity profile, and *m* and *n* are constants. The following observation can be made for the proposed sigmoid function: First, the sigmoid function is a monotonically increasing function, similar to the intensity profile of a blurred step edge. Second, the upper asymptote is the horizontal straight line with a value of $K+D$, which can be related to the maximum intensity of the image. Third, the lower asymptote is the horizontal straight line with a value of *D*, which can be related to the minimum intensity of the image. Fourth, the value of *x* that makes $mx+n$ equal to zero is assumed as the edge position, and the maximum slope is observed at this position in the case of the profile function. Fifth, as the magnitude of *m* decreases, the maximum slope decreases as in Eq. (2), which indicates that the edge is more blurred. Figure 5 shows a typical example of sigmoid function when m = -0.2, n = 10, K = 200, D = 25.

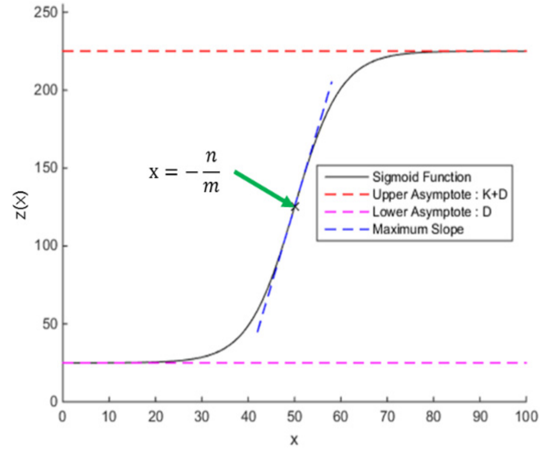

FIG. 5. Sigmoid function when *m* = -0.2, *n* = 10, *K* = 200, *D* = 25.

The main geometry of TFT-LCD patterns consists of shapes such as lines, circles, and ellipses. By expanding the above one-dimensional blurred edge model into 2D, the edge with the desired geometry can be calculated. For the case of line, circle, and ellipse geometry, the Eq. (1) can be expanded as Eqs. (3)~(5).

Line

$$Z(X,Y,\vec{\beta}_{line})=\frac{K}{1+\exp(aX+bY+c)}+D \tag{3}$$

Circle

$$Z(X,Y,\vec{\beta}_{circle})=\frac{K}{1+\exp(aX^2+aY^2+bX+cY+e)}+D \tag{4}$$

Ellipse

$$Z(X,Y,\vec{\beta}_{ellipse})=\frac{K}{1+\exp(aX^2+bY^2+cX+dY+eXY+f)}+D \tag{5}$$

where $\vec{\beta}$ is the model's coefficient vector and can be written as in Eq. (6) for a geometry of line, circle, and ellipse.

$$\vec{\beta}_{line}=\begin{bmatrix}K\\D\\a\\b\\c\end{bmatrix},\ \vec{\beta}_{circle}=\begin{bmatrix}K\\D\\a\\b\\c\\e\end{bmatrix},\ \vec{\beta}_{ellipse}=\begin{bmatrix}K\\D\\a\\b\\c\\d\\e\\f\end{bmatrix} \tag{6}$$

Figures 6~8 show the example of 2D sigmoid function for line, circle and ellipse geometry in top view and isometric view, respectively. Figure 6 shows the modeling

function $Z(X, Y, \vec{\beta}_{line})$, when the geometry function is $0.5\left(-x-\frac{2}{5}y+70\right)=0$. Figure 7 shows the modeling function $Z(X, Y, \vec{\beta}_{circle})$ when the geometry function is $0.01\{(x-50)^2+(y-50)^2-30^2\}=0$. Figure 8 shows the modeling function $Z(X, Y, \vec{\beta}_{ellipse})$ when the geometry function is $5\left\{\frac{\left(\cos\left(\frac{\pi}{4}\right)(x-50)+\sin\left(\frac{\pi}{4}\right)(y-50)\right)^2}{400}+\frac{\left(\cos\left(\frac{\pi}{4}\right)(x-50)-\sin\left(\frac{\pi}{4}\right)(y-50)\right)^2}{800}-1\right\}=0$.

Figures 6~8 show that the edge of an image follows the geometry function. The coefficients multiplied to the geometry function, 0.5, 0.01, 5 correspond to the degree of blur. For each geometry, the model's coefficient vector is

$$\vec{\beta}_{line}=\begin{bmatrix}200\\25\\-1/2\\-1/5\\35\end{bmatrix},\ \vec{\beta}_{circle}=\begin{bmatrix}200\\25\\1/100\\-1\\-1\\41\end{bmatrix},\ \vec{\beta}_{ellipse}=\begin{bmatrix}200\\25\\3/64\\3/64\\-25/8\\-25/8\\-1/32\\525/4\end{bmatrix} \quad (7)$$

In conclusion, not only the edge position but also the geometry function can be obtained by substituting the exponent term to any explicit form of geometry function. Thus, the blur model for an arbitrary geometry can be expressed as

$$Z(X, Y, \vec{\beta})=\frac{K}{1+\exp(T(X, Y, \vec{\gamma}))}+D \quad (8)$$

where $T(X, Y, \vec{\gamma})$ is the geometry function, $\vec{\gamma}$ is the coefficient vector of geometry function, and $\vec{\beta}$ is the blur model's coefficient vector. Therefore, the blur model's coefficient vector $\vec{\beta}$ is written as

$$\vec{\beta}=\begin{bmatrix}K\\D\\\vec{\gamma}\end{bmatrix} \quad (9)$$

2.3. Fitting Algorithm

As mentioned before, the proposed blur model can calculate the desired geometry function by modeling the blur. In this study, to find the model that fits the given image, the model's coefficient vector $\vec{\beta}$ is calculated by nonlinear fitting. From the $\vec{\beta}$, the geometry coefficient vector $\vec{\gamma}$ can finally be obtained. The nonlinear fitting is expressed as the least square error formulation as

$$\min_{\vec{\beta}}\left\{\sum_i\sum_j\left[Z_{i,j}-Z(X_{i,j}, Y_{i,j}, \vec{\beta})\right]^2\right\}\ (0\le i<p,\ 0\le j<q) \quad (10)$$

where $Z_{i,j}$ is the image intensity at (*i, j*) pixel and *p*, *q* is the size of ROI.

In this study, the Levenberg-Marquardt method is used, and that method needs the initial value for the iteration. The initial value of the model's coefficient vector is notated as $\vec{\beta}_0$, where

$$\vec{\beta}_0=\begin{bmatrix}K_0\\D_0\\\vec{\gamma}_0\end{bmatrix} \quad (11)$$

By using the characteristic of the sigmoid function, the K_0 and D_0 can be calculated as

$$D_0=\min_{(i,j)}\{Z_{i,j}\} \quad (12)$$

$$K_0=\max_{(i,j)}\{Z_{i,j}\}-D_0 \quad (13)$$

To calculate the initial value of geometry coefficient vector $\vec{\gamma}_0$, the geometry function $T(X, Y, \vec{\gamma})$ of Eq. (8) can be approximated as Eq. (14) by using the K_0, D_0, and the intensity of the image.

$$T(X_{i,j}, Y_{i,j}, \vec{\gamma})\approx\ln\left(\frac{K_0}{Z_{i,j}-D_0}-1\right) \quad (14)$$

where $\ln$ is the natural logarithm. Therefore, the least squares fitting method problem for the geometry function $T(X, Y, \vec{\gamma})$ can be defined as

$$\min_{\vec{\gamma}}\left\{\sum_i\sum_j\left[T(X_{i,j},Y_{i,j},\vec{\gamma})-\mathrm{Ln}Z_{i,j}\right]^2\right\}\ (0\le i<p,\ 0\le j<q) \quad (15)$$

where $X_{i,j}$ and $Y_{i,j}$ is pixel coordinate value at (*i, j*), and $\mathrm{Ln}Z_{i,j}=\ln\left(\frac{K_0}{Z_{i,j}-D_0}-1\right)$. For the line geometry, the least squares fitting problem can be written in matrix form as

$$\min_{\vec{\gamma}}\left\|\begin{bmatrix}\vec{X} & \vec{Y} & \begin{matrix}1\\1\\\vdots\\1\end{matrix}\end{bmatrix}\vec{\gamma}-\overrightarrow{\mathrm{Ln}Z}\right\|^2,\ where\ \vec{\gamma}=\begin{bmatrix}a\\b\\c\end{bmatrix}\ for\ line\ geometry \quad (16)$$

where $\vec{X}$, $\vec{Y}$ are the vectors of $X_{i,j}$ and $Y_{i,j}$, and $\overrightarrow{\mathrm{Ln}Z}$ is the vector of $\mathrm{Ln}Z_{i,j}$. The matrix Eq. (16) for the circle and ellipse geometry are given in more detail in the Appendix.

$$\vec{X}=\begin{bmatrix}X_{0,0}\\X_{0,1}\\\vdots\\X_{i,j}\\\vdots\\X_{p-1,q-1}\end{bmatrix},\ \vec{Y}=\begin{bmatrix}Y_{0,0}\\Y_{0,1}\\\vdots\\Y_{i,j}\\\vdots\\Y_{p-1,q-1}\end{bmatrix},\ \overrightarrow{\mathrm{Ln}Z}=\begin{bmatrix}\mathrm{Ln}Z_{0,0}\\\mathrm{Ln}Z_{0,1}\\\vdots\\\mathrm{Ln}Z_{i,j}\\\vdots\\\mathrm{Ln}Z_{p-1,q-1}\end{bmatrix} \quad (17)$$

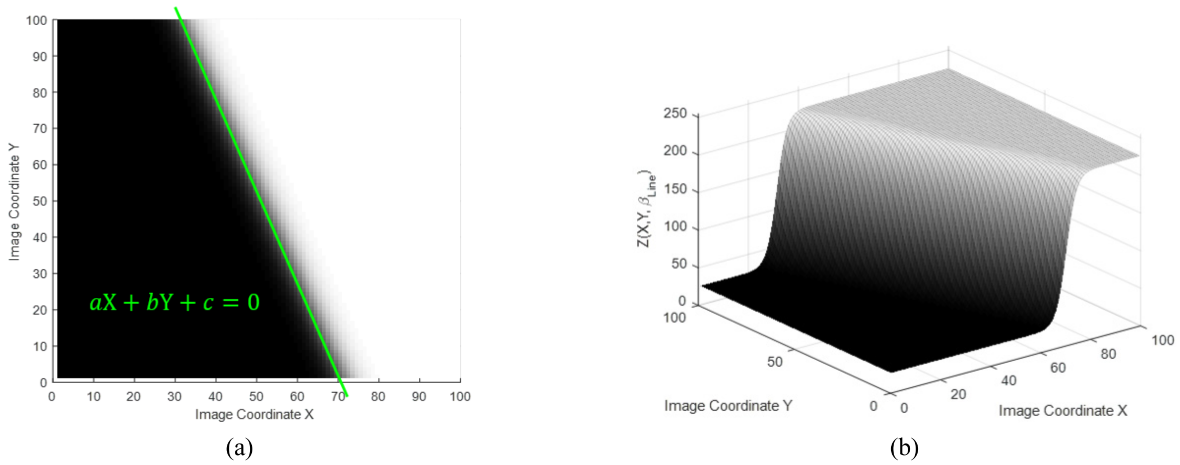

FIG. 6. 2D sigmoid function for line geometry when the geometry function is $0.5\left(-x-\frac{2}{5}y+70\right)=0$. (a) Top view of the function. (b) Isometric view of the function.

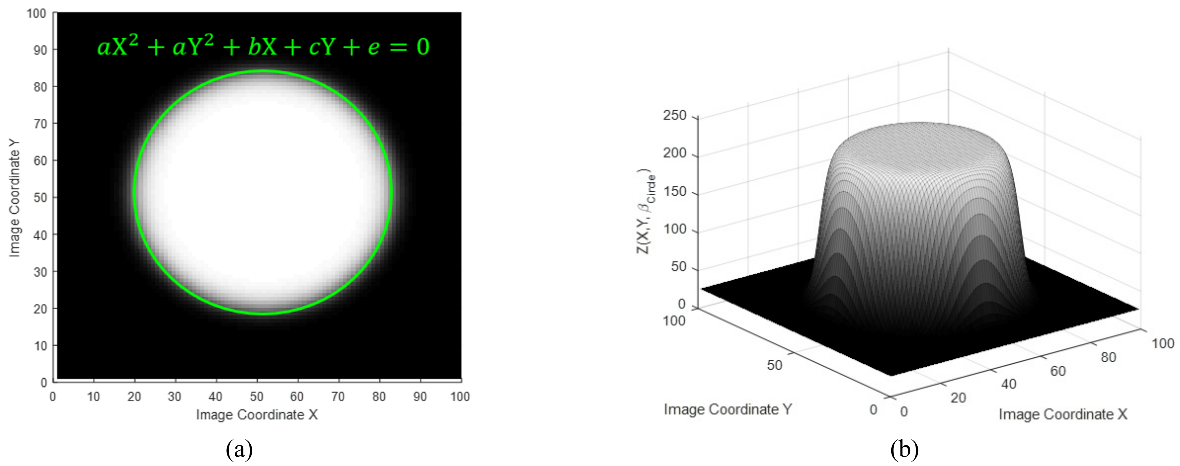

FIG. 7. 2D sigmoid function for circle geometry when the geometry function is $0.01\{(x-50)^2+(y-50)^2-30^2\}=0$. (a) Top view of the function. (b) Isometric view of the function.

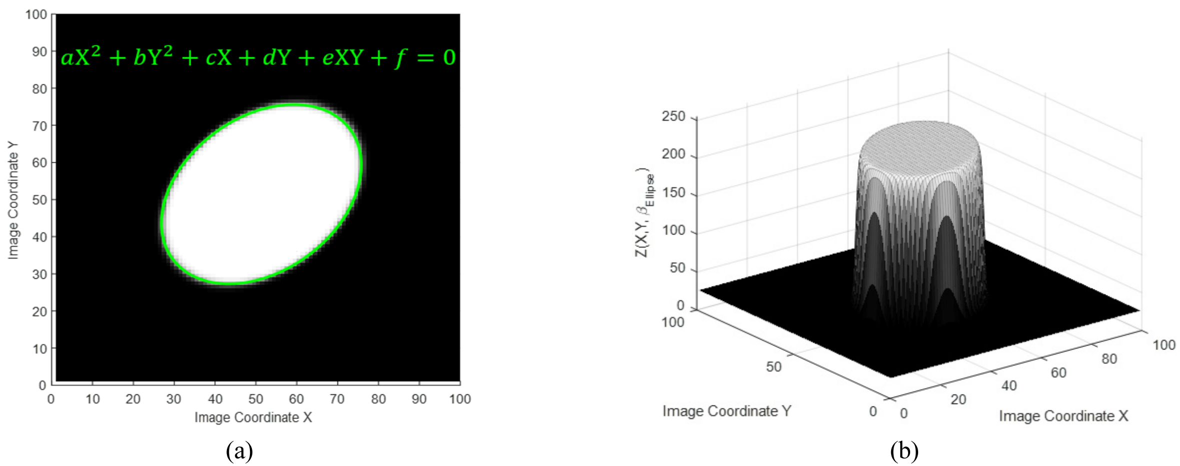

FIG. 8. 2D sigmoid function for ellipse geometry when $5\left\{\frac{\left(\cos\left(\frac{\pi}{4}\right)(x-50)+\sin\left(\frac{\pi}{4}\right)(y-50)\right)^2}{400}+\frac{\left(\cos\left(\frac{\pi}{4}\right)(x-50)-\sin\left(\frac{\pi}{4}\right)(y-50)\right)^2}{800}-1\right\}=0$. (a) Top view of the function. (b) Isometric view of the function.

Eq. (16) can be solved by differentiating the square norm part with $\vec{\gamma}$, and the result is as follows.

$$\frac{\partial|P\vec{\gamma}-\overrightarrow{LnZ}|^2}{\partial\vec{\gamma}}=2P^T(P\vec{\gamma}-\overrightarrow{LnZ})=0 \tag{18}$$

where $P=\begin{bmatrix} & & 1 \\ & & 1 \\ \vec{X} & \vec{Y} & \vdots \\ & & 1 \end{bmatrix}$

$$\text{Thus, } \vec{\gamma}=(P^TP)^{-1}P^T\overrightarrow{LnZ} \tag{19}$$

Finally, the initial value of geometry coefficient vector $\vec{\gamma}_0$ can be calculated from Eq. (19) and therefore, the initial value of model's coefficient vector $\vec{\beta}_0$ can be calculated. The Levenberg-Marquardt method converges by iterative operation using the following vector formula.

$$\vec{\beta}_{k+1}=\vec{\beta}_k+[J^TJ+\lambda\mathrm{diag}(J^TJ)]^{-1}J^T\left[\vec{Z}-Z(\vec{X},\vec{Y},\vec{\beta}_k)\right],\ k=1,2,3,... \tag{20}$$

where each term has the following meaning

$$\vec{Z}=\begin{bmatrix} Z_{0,0} \\ Z_{0,1} \\ \vdots \\ Z_{i,j} \\ \vdots \\ Z_{p-1,q-1} \end{bmatrix},\ Z(\vec{X},\vec{Y},\vec{\beta}_k)=\begin{bmatrix} Z(X_{0,0},Y_{0,0},\vec{\beta}_k) \\ Z(X_{0,1},Y_{0,1},\vec{\beta}_k) \\ \vdots \\ Z(X_{i,j},Y_{i,j},\vec{\beta}_k) \\ \vdots \\ Z(X_{p-1,q-1},Y_{p-1,q-1},\vec{\beta}_k) \end{bmatrix} \tag{21}$$

$$J=\frac{\partial Z(\vec{X},\vec{Y},\vec{\beta}_k)}{\partial\vec{\beta}_k}\quad (k\ th\ Jacobian\ Matrix) \tag{22}$$

$$\lambda : \text{Damping Factor} \tag{23}$$

$$\mathrm{diag}(A) : \text{Diagonal Vector of } A \tag{24}$$

If the damping factor λ is small, it behaves like the Gauss-Newton method. In this paper, λ is set to 0.0001 because both iteration speed and convergence stability are important for the in-line situation. The condition for convergence is set to the case when the change of the error becomes smaller than the specific value as shown Eq. (25).

$$\epsilon_k=\|Z_{X,Y}-Z(X,Y,\vec{\beta}_k)\|^2-\|Z_{X,Y}-Z(X,Y,\vec{\beta}_{k-1})\|^2<0.00001 \tag{25}$$

III. EXPERIMENT AND REULTS

3.1. Experimental System

To verify the proposed edge detection method, a general optical microscope system as shown in Fig. 9 is used. Also as in Fig. 10, to check the applicability of proposed method for various geometry, Indium Tin Oxide (ITO), Half-tone photoresist (HT-PR) and hole patterns (Hole A, Hole B) are used, where ITO and HT-PR are line geometry and Hole A and B are circle geometry.

In this optical system configuration, to obtain the best-focused image, image autofocus method using Gaussian focus value [12-15] is used. This method uses images,

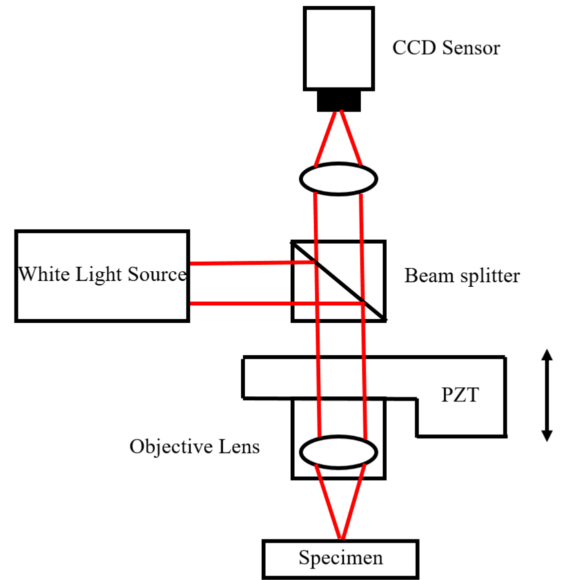

FIG. 9. General optical microscope system using the Piezo Transducer (PZT).

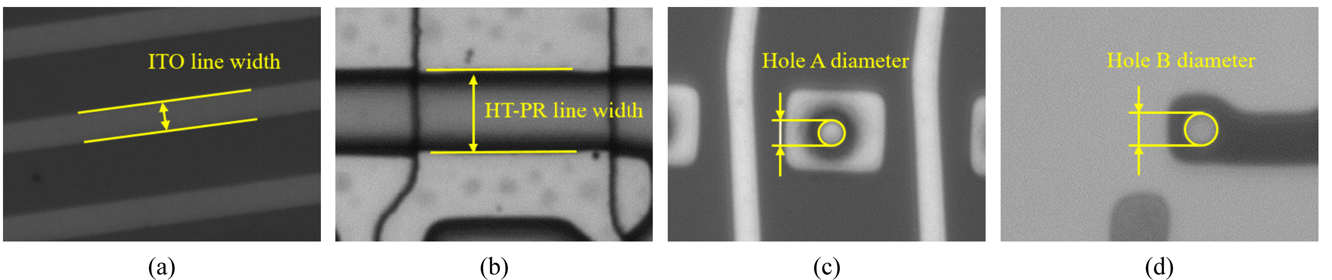

FIG. 10. Indium Tin Oxide (ITO), Half-tone photoresist (HT-PR) and hole pattern images. (a) ITO. (b) HT-PR. (c) Hole A. (d) Hole B.

captured in every focal step, which is produced by the vertical movement of piezo transducer (PZT). Each sample is repeatedly measured 20 times and compared with conventional edge detection method. Detail specification of the system is shown in Table 1. In Table 1, "Sampling" is the number of pixels in the image, and "Spatial Sampling" is the size of each pixel in micrometer unit. "Field of View" is the size of the image in micrometer unit.

3.2. Fitting Result

Using the proposed method, the fitting results for each pattern image are shown in Fig. 11. The number of iterations is less than 130 and the least square error between image intensity and fitting results is less than 5.56 for both line and circle pattern images. The goodness of fitting is verified by using the chi-square (χ^2) test as Eq. (26) [16]. The value of the χ^2 is derived from the number of objects n

TABLE 1. Specifications of the measurement system

Equipment	2D critical dimension measurement system	
Environment	Vibration class: VC-E	
PC specification	Processor	Intel(R) Xeon(R)
		CPU E3-1280 V2 @ 3.60 GHz (4 CPUs)
	RAM	8208MB RAM
Measurement condition	Objective lens	50× (2D)
	Sampling	1280 Pixel (H) × 1024 Pixel (V)
	Spatial sampling	0.110 μm × 0.110 μm
	Field of view	140.80 μm × 112.64 μm

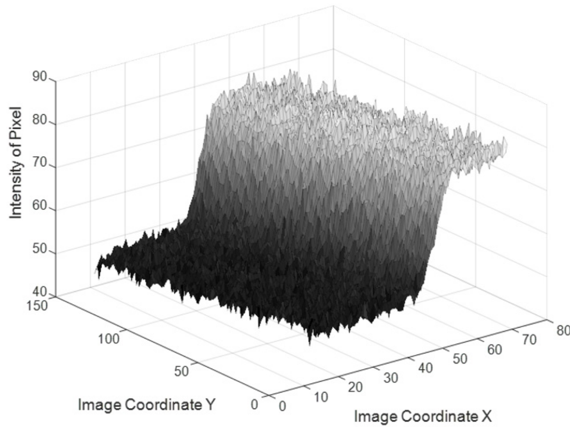

(a)

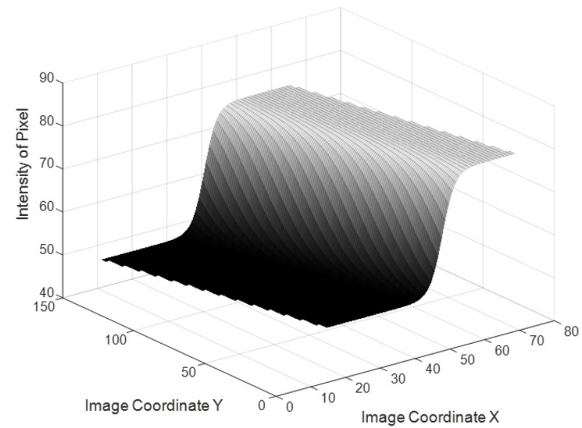

(b)

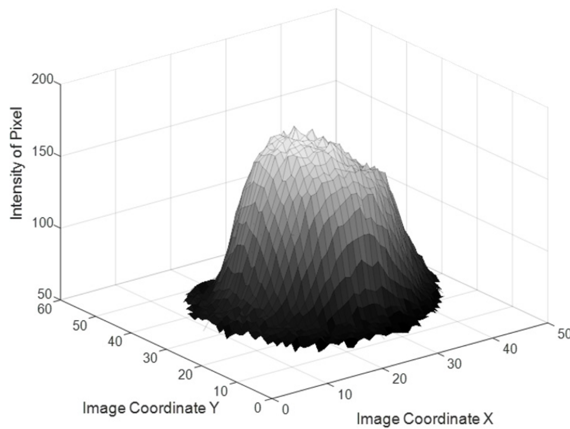

(c)

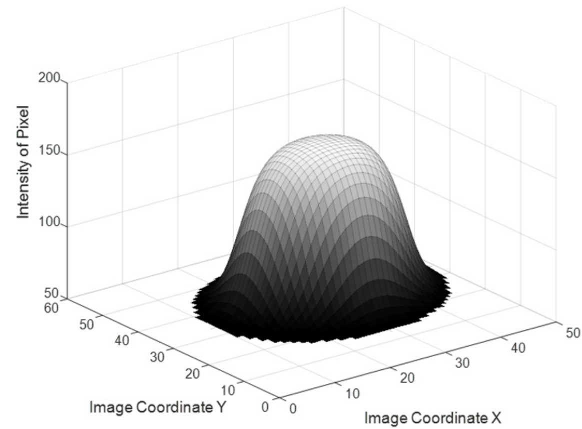

(d)

FIG. 11. Fitting results for line (ITO and HT-PR edge) and circle (Hole A and Hole B edge) pattern. (a) Original intensity of line image. (b) Fitting intensity of line image. (c) Original intensity of circle image. (d) Fitting intensity of circle image.

and confidence value α in the χ^2 distribution table. χ^2 value is 7105.69 in line geometry and 1356.11 in circle geometry when $\alpha = 0.05$ and n is the number of pixels in ROI. The actual modeling error is 258.73 in line geometry and 306.00 in circle geometry. Therefore, our proposed blur model can be confirmed to work well under the blurred and noisy environment.

$$\chi^2_{\alpha/2,n-1} > \sum_i \sum_j \frac{\left(Z_{i,j} - Z\left(X_{i,j}, Y_{i,j}, \vec{\beta}\right)\right)^2}{Z\left(X_{i,j}, Y_{i,j}, \vec{\beta}\right)} \quad (0 \le i < p,\ 0 \le j < q) \tag{26}$$

where $Z_{i,j}$ is image intensity and $Z\left(X_{i,j}, Y_{i,j}, \vec{\beta}\right)$ is fitting intensity at (i, j) pixel, and p, q is size of ROI.

3.3. Measurement Result

Tables 2(a) and 2(b) show the comparison of the measured results for the conventional LoG mask sub-pixel method [1], error function fitting method [7] and the proposed method. As both previous methods are only represented about a 1D intensity profile, circle geometry edge detection is performed by applying each method to the radial scan intensity profile at one-degree intervals. For both line and circle pattern geometry, the proposed method shows better repeatability. For the line geometry, the repeatability is about 3 times better than for the conventional LoG method and 1.6 times better than the error function method in the ITO sample. Also for the HT-PR sample, the repeatability is about 2 times better than the conventional LoG method and 3.5 times better than the error function method. For the circle geometry, the repeatability is about 2 times better than the conventional LoG method and 1.6~2 times better than the error function method. The computation time is observed to be less than 0.1s for all patterns, which implies that the proposed method can be applied to real-time inspection.

TABLE 2. CD measurement results from LoG mask sub-pixel method and sigmoid surface fitting method. (a) Measurement results of line width (ITO, HT-PR). (b) Measurement results of circle diameter (Hole A, B).

(a) Line width (unit: μm)

Sample	ITO			HT-PR		
Method	LoG mask sub-pixeling	Error function fitting	Sigmoid surface fitting	LoG mask sub-pixeling	Error function fitting	Sigmoid surface fitting
Average	2.243	2.243	2.241	8.466	8.467	8.461
3*STD	0.018	0.008	0.005	0.008	0.014	0.004
1	2.238	2.243	2.243	8.461	8.464	8.460
2	2.239	2.244	2.240	8.468	8.473	8.459
3	2.240	2.242	2.242	8.468	8.465	8.460
4	2.249	2.242	2.238	8.469	8.472	8.463
5	2.242	2.245	2.240	8.470	8.461	8.461
6	2.249	2.242	2.241	8.463	8.466	8.459
7	2.234	2.240	2.242	8.464	8.462	8.461
8	2.230	2.242	2.243	8.467	8.470	8.461
9	2.244	2.243	2.241	8.465	8.472	8.460
10	2.247	2.246	2.239	8.462	8.461	8.460
11	2.243	2.251	2.240	8.462	8.469	8.459
12	2.254	2.245	2.241	8.465	8.470	8.461
13	2.242	2.243	2.242	8.466	8.471	8.463
14	2.240	2.241	2.238	8.467	8.466	8.462
15	2.246	2.240	2.243	8.465	8.462	8.460
16	2.248	2.243	2.241	8.466	8.471	8.462
17	2.240	2.240	2.240	8.465	8.473	8.459
18	2.243	2.243	2.242	8.469	8.458	8.461
19	2.250	2.242	2.245	8.463	8.465	8.459
20	2.249	2.241	2.239	8.467	8.468	8.460

TABLE 2. CD measurement results from LoG mask sub-pixel method and sigmoid surface fitting method. (a) Measurement results of line width (ITO, HT-PR). (b) Measurement results of circle diameter (Hole A, B) (Continue).

(b) Circle diameter (unit: μm)

Sample	Hole A			Hole B		
Method	LoG mask sub-pixeling	Error function fitting	Sigmoid surface fitting	LoG mask sub-pixeling	Error function fitting	Sigmoid surface fitting
Average	2.862	2.872	2.866	2.764	2.760	2.758
3*STD	0.034	0.024	0.016	0.031	0.029	0.015
1	2.868	2.867	2.864	2.766	2.769	2.759
2	2.845	2.874	2.866	2.766	2.771	2.764
3	2.857	2.876	2.867	2.752	2.757	2.751
4	2.875	2.864	2.866	2.769	2.760	2.754
5	2.846	2.866	2.858	2.754	2.759	2.762
6	2.878	2.870	2.861	2.766	2.776	2.763
7	2.860	2.886	2.870	2.765	2.763	2.755
8	2.848	2.861	2.857	2.751	2.770	2.757
9	2.856	2.863	2.866	2.739	2.758	2.747
10	2.872	2.871	2.861	2.757	2.756	2.754
11	2.861	2.863	2.866	2.775	2.773	2.761
12	2.860	2.882	2.870	2.777	2.759	2.757
13	2.852	2.883	2.865	2.778	2.775	2.765
14	2.876	2.883	2.873	2.763	2.756	2.765
15	2.873	2.862	2.861	2.763	2.752	2.760
16	2.842	2.864	2.861	2.774	2.744	2.754
17	2.869	2.876	2.871	2.751	2.747	2.756
18	2.868	2.877	2.873	2.770	2.748	2.755
19	2.870	2.880	2.877	2.768	2.752	2.762
20	2.872	2.878	2.870	2.771	2.752	2.754

IV. CONCLUSION

In this paper, a more stable and precise edge detection method is proposed for measuring 2D CD of TFT-LCD pattern using a high magnification lens.

1) The optical blur of the edges of the image is modeled by using the proposed sigmoid function. From this new blurred edge modeling, the edge detection of images can also be performed.
2) By expanding the sigmoid blur edge model in two-dimensions and using the least squares fitting, the geometry information of the edge can be obtained mathematically. This method can be applied to various TFT patterns, and they can be expressed by a mathematically explicit formula.
3) The Levenberg-Marquardt method, a nonlinear fitting method, successfully applied for the surface fitting and it provides stable and fast results.
4) Compared with the existing LoG mask sub-pixel edge detection method, it is possible to measure with at least twice better repeatability, while the calculation time is observed as less than 0.1 seconds. Also in comparison with the error function method, it is confirmed that the measuring repeatability is at least 1.6 times better. It is confirmed that it can be successfully applied to the optical two-dimensional CD measurement system for TFT-LCD pattern.

APPENDIX

For circle and ellipse geometry, the Eq. (16) is written as follows.

Circle

$$\min_{\vec{\gamma}} \left\| \begin{bmatrix} \overrightarrow{X^2}+\overrightarrow{Y^2} & \vec{X} & \vec{Y} & \begin{matrix} 1 \\ 1 \\ \vdots \\ 1 \end{matrix} \end{bmatrix} \vec{\gamma} - \overrightarrow{\mathrm{LnZ}} \right\|^2, \; where \; \vec{\gamma} = \begin{bmatrix} a \\ b \\ c \\ e \end{bmatrix} \tag{27}$$

Ellipse

$$\min_{\vec{\gamma}} \left\| \begin{bmatrix} \overrightarrow{X^2} & \overrightarrow{Y^2} & \vec{X} & \vec{Y} & \overrightarrow{XY} & \begin{matrix} 1 \\ 1 \\ \vdots \\ 1 \end{matrix} \end{bmatrix} \vec{\gamma} - \overrightarrow{LnZ} \right\|^2, \ where \ \vec{\gamma} = \begin{bmatrix} a \\ b \\ c \\ d \\ e \\ f \end{bmatrix} \quad (28)$$

where $\overrightarrow{X^2}$, $\overrightarrow{Y^2}$ and $\overrightarrow{XY}$ are defined as follows.

$$\overrightarrow{X^2} = \begin{bmatrix} X_{0,0}^2 \\ X_{0,1}^2 \\ \vdots \\ X_{i,j}^2 \\ \vdots \\ X_{p-1,q-1}^2 \end{bmatrix}, \ \overrightarrow{Y^2} = \begin{bmatrix} Y_{0,0}^2 \\ Y_{0,1}^2 \\ \vdots \\ Y_{i,j}^2 \\ \vdots \\ Y_{p-1,q-1}^2 \end{bmatrix}, \ \overrightarrow{XY} = \begin{bmatrix} X_{0,0}Y_{0,0} \\ X_{0,1}Y_{0,1} \\ \vdots \\ X_{i,j}Y_{i,j} \\ \vdots \\ X_{p-1,q-1}Y_{p-1,q-1} \end{bmatrix} \quad (29)$$

The equations for these geometries are also calculated by the same method as used in Eqs. (18) and (19).

REFERENCES

1. S.-H. Park, J.-H. Lee, and H. J. Pahk, "In-line critical dimension measurement system development of LCD pattern proposed by newly developed edge detection algorithm," J. Opt. Soc. Korea **17**(5), 392-398 (2013).
2. N.-T. Doan, J. H. Moon, T. W. Kim, H. J. Pahk, "A fast image enhancement technique using a new scanning path for critical dimension measurement of glass panels," Int. J. Precis. Eng. Manuf. **13**, 2109-2114 (2012).
3. N. Xu and Y.-T. Kim, "An image sharpening algorithm for high magnification image zooming," In *Consumer Electronics* (ICCE) (2010 Digest of Technical Papers International Conference on. IEEE), pp. 27-28.
4. A. J. Tabatabai and O. R. Mitchell, "Edge location to subpixel values in digital imagery," IEEE Trans. Pattern Anal. Mach. Intell. **2**, 188-201 (1984).
5. Q. Sun, Y. Hou, Q. Tan, C. Li, and M. Liu, "A robust edge detection method with sub-pixel accuracy," Optik - International Journal for Light and Electron Optics **125**(14), 3449-3453 (2014).
6. J. Ye, G. Fu, and U. P. Poudel, "High-accuracy edge detection with blurred edge model," Image Vis. Comput. **23**(5), 453-467 (2005).
7. M. Hagara and P. Kulla, "Edge detection with sub-pixel accuracy based on approximation of edge with Erf function," Radioengineering **20**(2), 516-524 (2011).
8. G.-S. Xu, "Sub-pixel edge detection based on curve fitting," In *Information and Computing Science* (2009. ICIC'09. Second International Conference on. IEEE), pp. 373-375.
9. I. Sobel, "Neighborhood coding of binary images for fast contour following and general binary array processing," Comput. graphics image process. **8**(1), 127-135 (1978).
10. A. Huertas and G. Medioni, "Detection of intensity changes with subpixel accuracy using Laplacian-Gaussian masks," IEEE Trans. Pattern Anal. Mach. Intell. **5**, 651-664 (1986).
11. J. Canny, "A computational approach to edge detection," IEEE Trans. Pattern Anal. Mach. Intell. **6**, 679-698 (1986).
12. T. T. E. Yeo, S. H. Ong, and R. Sinniah, "Autofocusing for tissue microscopy," Image Vis. Comput **11**(10), 629-639 (1993).
13. D. L. Marks, A. L. Oldenburg, J. J. Reynolds, and S. A. Boppart, "Autofocus algorithm for dispersion correction in optical coherence tomography," Appl. Opt. **42**(16), 3038-3046 (2003).
14. S. H. Fox, R. M. Silver, E. Kornegay, and M. Dagenais, "Focus and edge detection algorithms and their relevance to the development of an optical overlay calibration standard," In *Microlithography'99* (International Society for Optics and Photonics, 1999), pp. 95-106.
15. J.-H. Ahn, J. Ko, I. Y. Lee, and S. H. Kim, "A fast continuous auto focus algorithm using the state transition model," Pac. Sci. Rev. **13**, 125-130 (2011).
16. R. L. Plackett, "Karl Pearson and the Chi-squared test," Int. Stat. Rev. **51**, 59-72 (1983).